Geophysical Research Letters

RESEARCH LETTER
10.1029/2021GL096119

Double Diffusion As a Driver of Turbulence in the Stratified Boundary Layer Beneath George VI Ice Shelf

L. Middleton[1,2], P. E. D. Davis[2], J. R. Taylor[1], and K. W. Nicholls[2]

[1]Department of Applied Mathematics and Theoretical Physics, University of Cambridge, Centre for Mathematical Sciences, Cambridge, UK, [2]British Antarctic Survey, Cambridge, UK

Key Points:

- Year-long borehole mooring data in the George VI Ice Shelf ice-ocean boundary layer are analyzed
- Observed dissipation rates do not vary with mean-flow speed suggesting turbulence is not shear-driven
- Double-diffusive convection can explain the observed dissipation rates and melt rates, providing a route for parameterization

Supporting Information:

Supporting Information may be found in the online version of this article.

Correspondence to:

L. Middleton,
middleton.leo@gmail.com

Citation:

Middleton, L., Davis, P. E. D., Taylor, J. R., & Nicholls, K. W. (2022). Double diffusion as a driver of turbulence in the stratified boundary layer beneath George VI Ice Shelf. *Geophysical Research Letters*, *49*, e2021GL096119. https://doi.org/10.1029/2021GL096119

Received 16 SEP 2021
Accepted 14 FEB 2022

Abstract Warmer and more persistent intrusions of Circumpolar Deep Water (CDW) onto the West Antarctic Peninsula are a key driver of the recent increase in ice shelf mass loss. The relatively warm and salty CDW is thought to be mixed up to the base of the ice shelves via shear-driven turbulence where it has a high capacity to melt the ice. We analyze data from a year-long mooring beneath George VI Ice Shelf at a location where double-diffusive layering was observed. The turbulent dissipation rates do not vary with mean flow speed, suggesting shear-driven mixing is not the driver of basal melt at this site. Instead, we predict the observed dissipation using a new method that links along-isopycnal stirring of temperature anomalies with double-diffusive convection. Our work suggests that along-isopycnal temperature variance may be a stronger indicator of melt than flow speed within strongly stratified ice shelf-ocean boundary layers.

Plain Language Summary Recently, warmer water has reached West Antarctic ice shelves (the floating extensions of the ice sheet), for longer periods, leading to an increased ice melt. Predicting how changing ocean conditions alter melting is key to understanding the response of the Antarctic ice sheet to global warming, which affects the extent of sea-level rise. Basal melting is enhanced when warm and salty water is mixed up to the base of the ice. Often this mixing is forced by turbulence driven by the movement of water past the ice base. In this paper we analyze a year-long mooring data set beneath George VI Ice Shelf and find that the measured turbulence does not correlate with the flow speed. We find instead that the turbulence can be explained by variations in temperature and salinity. These variations in temperature and salinity can create unstable density gradients due to the different rates of molecular diffusion between heat and salt, hence the name "double diffusion'. Unstable gradients in density can then force turbulence that mixes heat and salt up to the ice. If the mixing of heat and salt depends temperature and salinity variations rather than flow speed, it may affect predictions of ice melt.

1. Introduction

Over recent decades ice mass loss from Antarctica has been the most dramatic on the West Antarctic Peninsula (Rignot et al., 2019). This is primarily due to warmer and more persistent intrusions of Circumpolar Deep Water onto the continental shelf (Jenkins et al., 2018). Circumpolar Deep Water is particularly warm ($\sim 1-2°C$) with a high capacity to melt ice. Circumpolar Deep Water is also relatively dense, due to its high salinity (~34.5–34.7 g/kg), leading Circumpolar Deep Water to intrude at depth beneath ice shelves. Turbulent processes flux heat upwards toward the ice, causing enhanced melting. In many locations, turbulence is driven by shearing flow past the ice (Davis & Nicholls, 2019; Jenkins et al., 2010). Within regional ice shelf cavity models, a parameterization is used that relates the melt rate to the velocity some distance away from the ice (Dinniman et al., 2016; Holland & Jenkins, 1999).

The most common parameterization is the "three-equation model" (Hellmer & Olbers, 1989; Holland & Jenkins, 1999). This couples budgets for heat and salt with a phase change condition that relates the freezing temperature of water to the salinity and pressure at the ice boundary,

$$F_m^T = F_i^T + F_O^T, \tag{1}$$

$$F_m^S = F_i^S + F_O^S, \tag{2}$$

$$T_b = \lambda_1 S_b + \lambda_2 + \lambda_3 P. \tag{3}$$

Here S_b and T_b are the boundary salinity and temperature, P the pressure and $\lambda_{1,2,3}$ are constants. F_m represents fluxes from melting (i.e., latent heat and freshwater flux), F_i represents fluxes from the ice (usually neglected for ice shelves, Holland & Jenkins, 1999) and F_O represents fluxes from the ocean. Ocean fluxes F_O^T and F_O^S are the focus of the parameterization. Models and observations often assume these fluxes are linearly related to the difference between far field and boundary values (i.e., $F_O^T \propto \Delta T = T_\infty - T_b$ and $F_O^S \propto \Delta S = S_\infty - S_b$), and depend on the far-field mean flow speed $\overline{U}$ (usually linearly i.e., $F_O^T, F_O^S \propto \overline{U}$). More complex parameterizations account for the turbulence-damping effects of stratification (M. G. McPhee et al., 1987; Vreugdenhil & Taylor, 2019), but a linear relationship to ΔT, ΔS, and $\overline{U}$ is often assumed (Dinniman et al., 2016), with proportionality constants constrained by observations (Malyarenko et al., 2020). We will refer to the combination of Equations 1–3 with linear parameterizations for the ocean fluxes F_O^T and F_O^S as the "three-equation formalism".

Davis and Nicholls (2019) presented turbulence mooring data collected beneath Larsen C Ice Shelf in 2012. Their data were consistent with a shear-driven boundary layer, varying with the tidal cycle (M. McPhee, 2008). Davis and Nicholls (2019) found that the three-equation formalism gave accurate melt rates using similar proportionality constants to Jenkins et al. (2010). In this letter we will consider data collected beneath George VI Ice Shelf (GVIIS) in the same 2012 field campaign as the Larsen C data using the same sampling techniques (see Figures 1a and 1b). The effects of stratification on turbulence underneath Larsen C were thought to be weak (Davis & Nicholls, 2019). However, the stratification observed underneath GVIIS is much stronger, extending up into the boundary layer (Kimura et al., 2015; Venables et al., 2014), shown in Figures 1c and 1d.

The effect of stratification on the ice shelf-ocean boundary layer has been investigated in simulations (Vreugdenhil & Taylor, 2019) and in data collected beneath sea-ice (Holland & Jenkins, 1999; M. G. McPhee et al., 1987). In these studies, stratification acts to damp shear-driven turbulence, and this effect can be modeled using the self-similarity theory of Monin and Obukhov (1954). However, beneath GVIIS, Conductivity, Temperature, Depth (CTD) profiles taken via the boreholes in the 2012 field campaign suggest a more complex role for stratification (Kimura et al., 2015; Venables et al., 2014). Persistent layers in temperature (T) and salinity (S) in the 20 m directly beneath the ice were found (shown in Figure 1d inset). This was the first time layering had been observed directly adjacent to the base of an ice shelf, however the number of observations beneath ice shelves is limited. Kimura et al. (2015) suggested the observed T/S layering was due to double-diffusive convection, where the differences in molecular diffusivity for heat and salt enable the release of potential energy. Active double-diffusive convection suggests that stratification may act to enhance boundary layer turbulence, rather than damping it. Within quiescent under-ice shelf regimes, Begeman et al. (2018) and Stevens et al. (2020) both suggested the presence of double-diffusive convection away from the boundary layer, but so far limited evidence of this has been presented.

Kimura et al. (2015) suggest layers adjacent to the ice are formed by "melt-driven convection', where destabilizing temperature gradients near the ice base drive convection, overcoming salinity gradients due to the faster diffusion of heat compared with salt. This theory is supported by Large-Eddy-Simulations from Rosevear et al. (2021), who found layers developing due to melt-driven convection in their simulations of a sheared, stratified ice-ocean boundary layer. Similar simulations were conducted by Middleton, Vreugdenhil, et al. (2021) with no ambient stratification or shearing, where turbulence was forced isotropically to match observed dissipation rates. Middleton, Vreugdenhil, et al. (2021) found persistent double-diffusive convection in a "George VI-like" parameter regime, without layers forming, suggesting layers are not necessary for the presence of double-diffusive convection beneath an ice shelf. Although layering is a possible signifier of double-diffusive convection in the ocean, double diffusion can impact turbulent flows without distinct layers forming (e.g., Dadonau et al., 2020; Konopliv & Meiburg, 2016). Indeed, Venables et al. (2014) showed that evidence of layering was absent from some of the CTD casts taken beneath GVIIS, suggesting layers may be intermittent. Using mooring data, it is difficult to confirm the presence or absence of layers and, even if we could, double-diffusive convection may occur in the absence of layers, as we have discussed. In this letter we apply a framework recently developed by Middleton and Taylor (2020) and Middleton, Fine, et al. (2021) to estimate the dissipation rate associated with double-diffusive processes without relying on the presence of thermohaline layers.

In our analysis of the GVIIS mooring data in Section 2, we find that kinetic energy dissipation rates do not vary with mean flow speed, unlike in the data from beneath Larsen C (Davis & Nicholls, 2019). The data from GVIIS are not consistent with a shear-driven boundary layer, or the assumption that heat and salt fluxes are related to

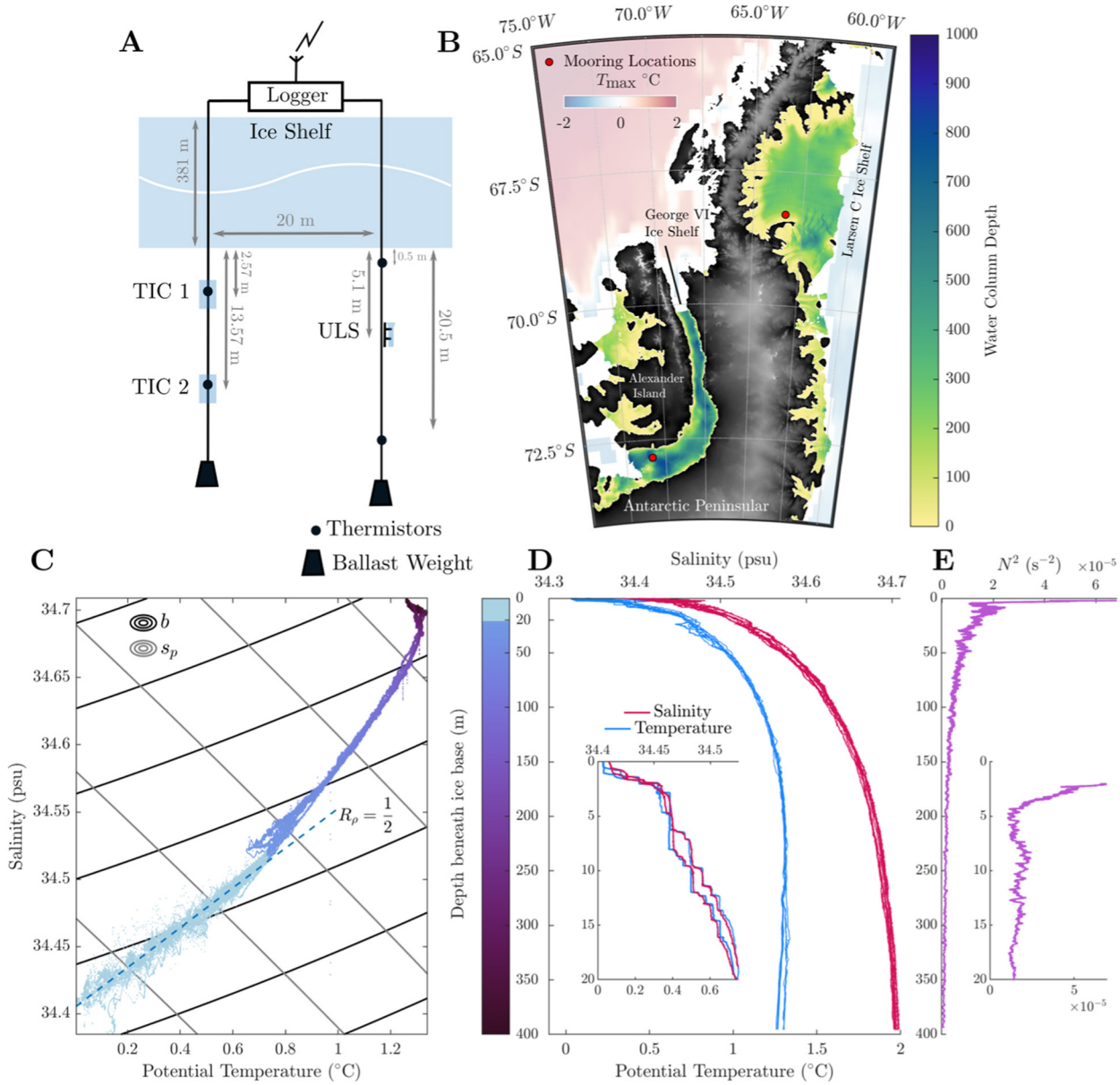

Figure 1. (a) Schematic of mooring. (b) Location of moorings. Maximum ocean temperature data taken from WOA decadal climatology (Locarnini et al., 2018). Water column depth taken from BedMachine (Morlighem et al., 2020). (c) Temperature/Salinity plot of 34 Conductivity, Temperature, Depth (CTD) casts. Upper 20 m highlighted as location of thermohaline staircase and $R_\rho = 1/2$ relationship given by dashed line. Buoyancy (b) contours are in black, and spice (s_p) contours are in gray. (d) CTD profiles including inset of upper 20 m for selected profiles. (e) Mean buoyancy frequency N^2 across CTD casts, smoothed with 2 m moving average.

far-field velocity in the three-equation formalism. However, turbulence is still present and drives a melt rate of 1.4 m yr^{-1}.

To explain the observed turbulence, we use the method of Middleton, Fine, et al. (2021) (M21) which hypothesizes that double-diffusive convection is linked to along-isopycnal stirring of temperature and salinity. At small-scales, diffusion of the resulting temperature and salinity gradients from along-isopycnal stirring causes an up-gradient diapycnal buoyancy flux that drives turbulence. We apply the M21 method using thermistor temperature measurements taken every ~20 min (5 min each side of the 15 min MAVS burst), and the predicted dissipation rates compare favorably to the observed dissipation rates throughout the year-long mooring timeseries. This suggests that heat and salt fluxes associated with double diffusion could be driving the observed melting.

In this letter, we first present the details of the mooring measurements beneath GVIIS. We show that dissipation rates beneath GVIIS do not depend on mean flow speed, in contrast to the assumption of shear-driven heat flux in the three-equation formalism and the data from beneath Larsen C Ice Shelf (Davis & Nicholls, 2019). In the third section we introduce the M21 method and show that observed dissipation rates beneath GVIIS can be explained by the stirring of temperature and salinity variance along isopycnals. Finally, in the fourth section we show that our hypothesis of a double-diffusive boundary layer is consistent with the observed heat flux through the boundary layer and the observed melt rates.

2. Observations

Two access holes, 20 m apart, were drilled using hot water, through GVIIS (S 72° 49.9′, W 070° 50.6′, see Figure 1a) in January 2012. Multiple CTD profiles were taken through both holes over a 5 day period, as well as microstructure profiles of temperature and velocity, reported on by Venables et al. (2014) and Kimura et al. (2015). A mooring was then deployed that operated for a period of 358 days. Using the first hole, Turbulence Instrument Clusters (TIC), consisting of Modular Acoustic Velocity Sensors (MAVS), thermistors and MicroSquid temperature sensors, were installed at 2.57 and 13.57 m beneath the ice base (identified at 333.4 dbar). In the second access hole, (ice base identified at 334.8 dbar), a thermistor chain was installed, with 11 thermistors (we only use two at 20.5 and 0.5 m, shown in Figure 1a), and an Upward-Looking Sonar (ULS) was installed 5.1 m beneath the ice base. The upward-looking sonar is only able to resolve melt rate variations over biweekly time scales, so correlations between melt rate and other variables are difficult to analyze, and we will use only the yearly melt rate estimate in this study. The ice thickness was 381.2 m, with a water column depth of 636.3 m.

The water column was strongly stratified, with a maximum temperature of 1.29°C and maximum salinity 34.71 (see Figure 1), suggestive of lower Circumpolar Deep Water (Moffat et al., 2009). The melt rate averaged 1.4 m yr^{-1} over the year-long mooring, varying between around 0.5 and 3 m yr^{-1} on weekly timescales, consistent with previous estimates for GVIIS (Bishop & Walton, 1981; Corr et al., 2002; Jenkins & Jacobs, 2008).

The MAVS sampled in 15 min bursts every 2 hr, providing dissipation estimates and mean flow speeds averaged over a 15 min period. Mean flow speeds vary between 0.5 and 13 cm s^{-1} (see Figure 2a), which overlaps with the wider range of speeds of between 1 and 25 cm s^{-1} beneath Larsen C (Davis & Nicholls, 2019). There was no strong spring-neap tidal cycle visible, unlike beneath Larsen C; however significant diurnal (K1, O1) and semi-diurnal (S2, M2) tides are present, consistent with data from Potter and Paren (1985).

We found an inertial subrange ($k^{-5/3}$ wavenumber slope) in the horizontal kinetic energy spectra (shown in Figures 3a and 3c) derived from the MAVS. Since the water column was strongly stratified, this is suggestive of a "stratified turbulence' regime (Lindborg, 2006), as opposed to unstratified three-dimensional turbulence assumed in Davis and Nicholls (2019). We used the Lindborg (2006) scaling to estimate dissipation rates (further details of our instrumentation and methodology are given in Supporting Information S1). The dissipation rate $\epsilon = \nu \overline{\frac{\partial u_i'}{\partial x_j}^2}$ is shown in Figure 2, panels B and C, as a function of the mean flow speed $\overline{u}$. The averaging operator $\bar{\cdot}$ denotes an average over the 15 min sampling burst. We find no significant correlation between mean flow speed and dissipation rate at either the upper or lower MAVS, in contrast to the data from Davis and Nicholls (2019). The dissipation rates in the GVIIS data are significantly reduced compared with the Larsen C data for the same mean flow speeds. There is also a lack of correlation between the Reynolds stress-based estimate of the friction velocity $u^* = \left(\overline{u'w'}^2 + \overline{v'w'}^2\right)^{1/4}$ (M. McPhee, 2008; Davis & Nicholls, 2019) and the mean flow speed (see Figure 2d). The prime $'$ denotes a departure from the 15 min burst mean, such that $u = \overline{u} + u'$. This suggests that a constant drag coefficient $C_d = \overline{u}^2/u^{*2}$ model for the friction velocity is inappropriate at this location.

Within the ice-ocean boundary layer, previous observations have found evidence for three distinct layers: the viscous sublayer close to the ice where the flow is laminar; the "surface layer" where rotation is unimportant and shear turbulence dominates the flow; and the "outer layer" where rotation and shear are important (M. McPhee, 2008). The depth of the surface and outer layers scale with the planetary length scale $u^*/|f|$ for f the Coriolis parameter. Empirical scaling constants have been suggested from observations, giving $0.05u^*/|f|$ for the surface layer (Davis & Nicholls, 2019) and $0.23u^*/|f|$ for the outer layer (Fer & Sundfjord, 2007). The outer layer width may also be controlled by stratification, in which case, the empirical scaling becomes $1.5u^*/\sqrt{|f|N_{pyc}}$ as

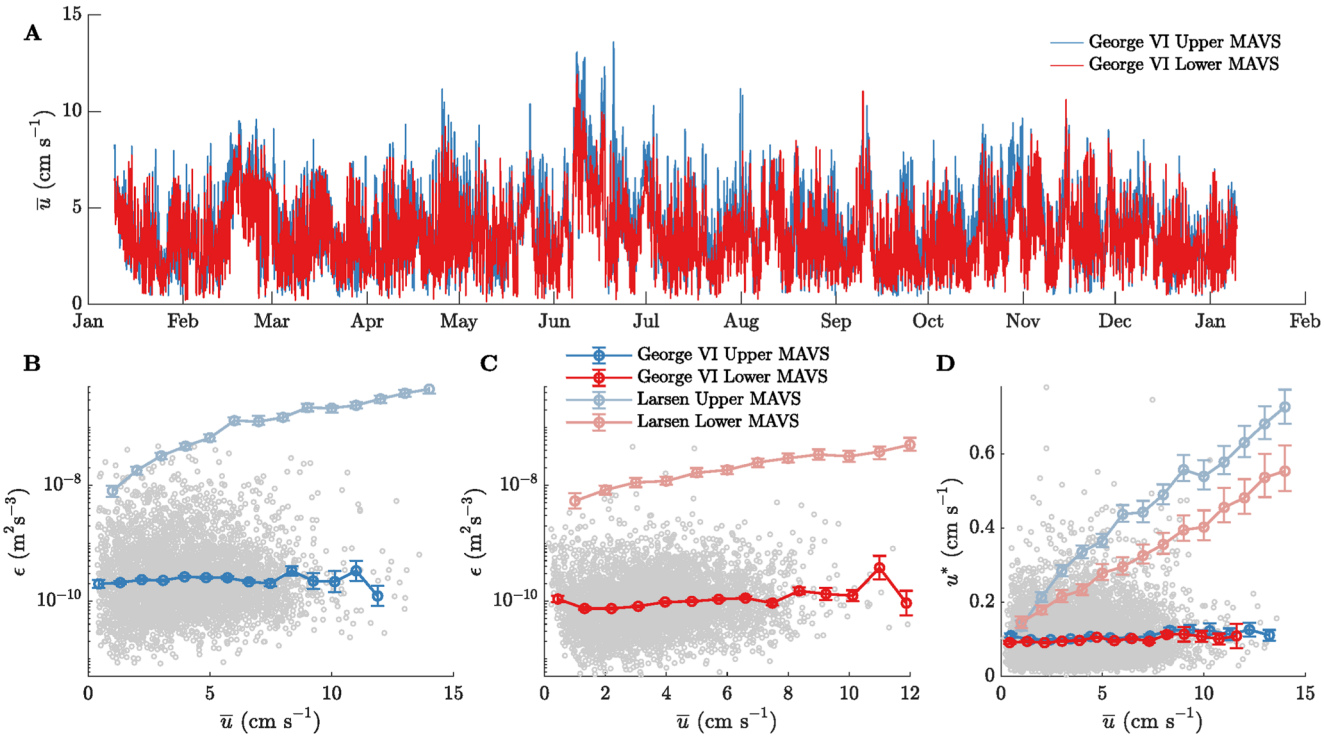

Figure 2. (a) Mean flow speed $\bar{u}$ timeseries for upper and lower Modular Acoustic Velocity Sensors (MAVS). (b) upper MAVS velocity against dissipation rate (burst estimates in gray) for George VI Ice Shelf (GVIIS) mooring data, Larsen C Ice Shelf mooring data included for comparison. (c) Same as B but for lower MAVS. (d) Friction velocity estimate $u^* = \left(\overline{u'w'}^2 + \overline{v'w'}^2\right)^{1/4}$ based on constant stress boundary layer for GVIIS upper and lower MAVS data (burst estimates in gray).

shown in Fer and Sundfjord (2007). If we assume a constant-stress boundary layer, we can apply the u^* estimate in Figure 2d to give a length scale $u^*/|f| = 7.5 \pm 5.3$ m where $\pm$ indicates one standard deviation. This gives a surface layer depth of $0.05u^*/|f| = 0.38 \pm 0.27$ m and an "outer layer" depth of $0.23u^*/|f| = 1.73 \pm 1.23$ m, which reaches the upper MAVS during periods of large u^* ($u^* > 0.15$ cm s^{-1}). Averaging the buoyancy frequency across the near-ice stratification (the top 5 m) observed in CTD profiles shown in Figure 1e, we can estimate the stratification-controlled outer layer depth as $1.5u^*/\sqrt{|f|N_{pyc}} = 1.77 \pm 1.25$ m, similar to the rotation-controlled estimate. We find no evidence of correlation between dissipation rate and mean flow speed even when only considering large u^* values (not shown). The possibility of shear-driven turbulence above our upper MAVS cannot be ruled out. However, in the absence of double diffusion we would expect shear-driven turbulence at the upper MAVS, which is not observed.

In Figure 3, panels A and C, we show the power spectral density for horizontal kinetic energy (as defined in Lindborg, 2006), averaged over mean flow speed, plotted against wavenumber, inferred from Taylor's "frozen field hypothesis" (see Supporting Information S1 for details). The frozen field hypothesis is only considered valid when $u'_{\text{rms}} \ll \bar{u}$ (Bluteau et al., 2011), which holds throughout our data. There is evidence of a $k^{-5/3}$ slope at low wavenumbers as mentioned above. In stratified turbulence, the power spectrum for horizontal kinetic energy is given by $E_{k_h} = 0.49\epsilon^{2/3}k^{-5/3}$ (Lindborg, 2006). The kinetic energy spectra at low wavenumbers collapse onto the same $k^{-5/3}$ line when bin-averaged by $\bar{u}$ (Figures 2a and 2c), indicating a lack of correlation between dissipation rate and mean flow speed. The wavenumber ranges in which there is instrumental noise (see Supporting Information S1) are shaded and the data in these regions are not included in our analysis. When the power spectrum for horizontal kinetic energy is averaged based on inferred dissipation rate within each burst (Figures 2b and 2d), the spectra no longer collapse, demonstrating the variation in turbulence levels across the data collection period.

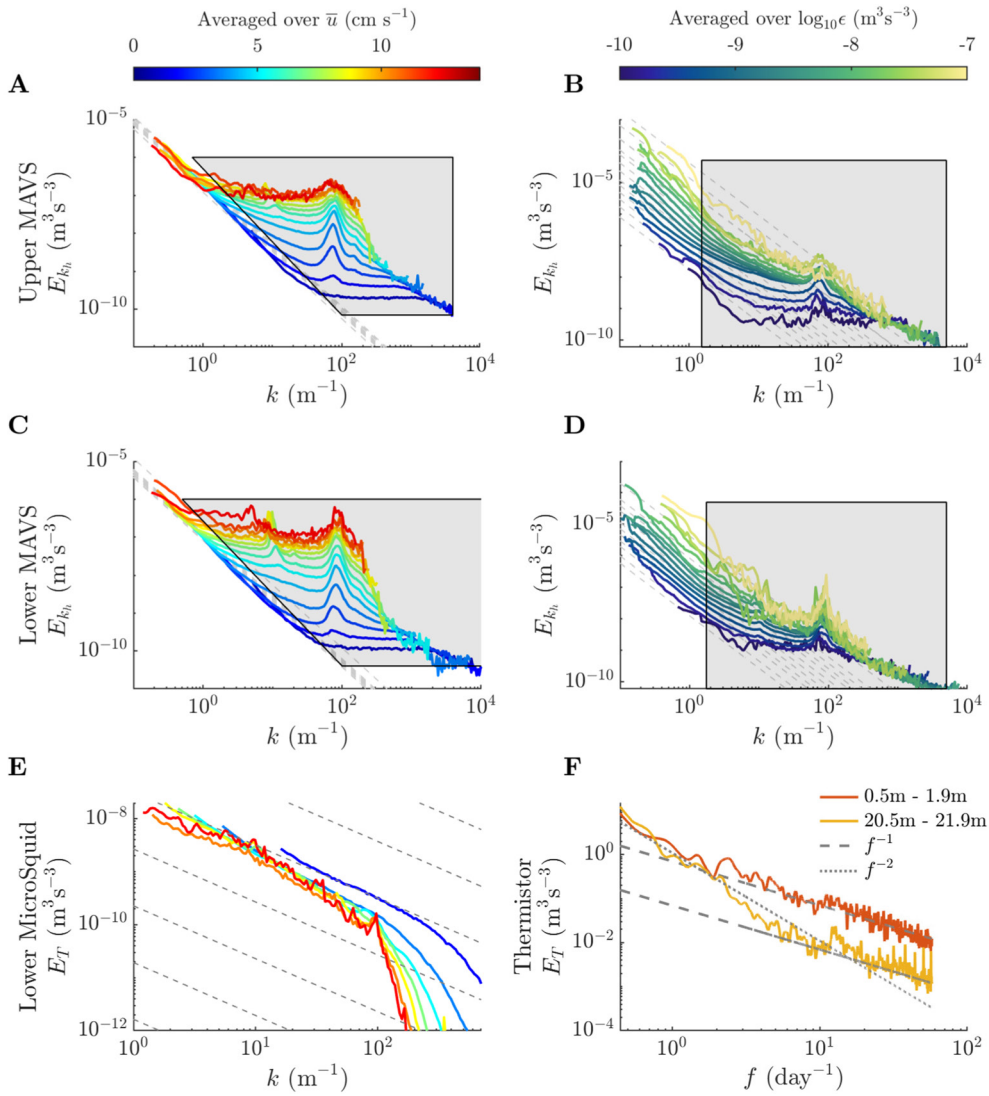

Figure 3. (a, c) Power spectral density of horizontal velocity fluctuations against wavenumber k, averaged by mean flow speed for upper and lower Modular Acoustic Velocity Sensors. Gray box represents a $f = 0.01$ frequency cutoff. (b, d) Same as a, c but averaged by burst-estimated dissipation rate. (e) Power spectral density of temperature fluctuations from lower MicroSquid thermistor, against wavenumber k, averaged by mean flow speed. Dashed lines indicate a k^{-1} slope. (f) Power spectral density of temperature fluctuations from thermistor chain, against frequency f over the full timeseries.

3. Double Diffusive Model

To explain the variation in dissipation rate ϵ, we will investigate an alternative driver for turbulence in the ice shelf-ocean boundary layer: double-diffusive convection. Double-diffusive convection is a term for a form of convection (a release of potential energy), facilitated by the difference in molecular diffusivities of heat and salt. Double-diffusive convection is a turbulent mixing process driven by gradients in temperature and salinity. However, this mixing process must be resupplied with heat and salt in order to maintain itself. Middleton, Fine, et al. (2021) suggested that the stirring of spice, $s_p = \alpha T + \beta S$ (α and β are the coefficients of thermal expansion and haline contraction), along isopycnals could be a generic mechanism for the supply of compensated gradients in temperature and salinity that drive double diffusion at small scales. They used this principle to develop a method to estimate small-scale double-diffusive buoyancy fluxes that force turbulence, using CTD data. We apply the M21 method to predict rates of double-diffusive convection in our mooring data using only coarsely sampled thermistor data and the T/S relation from the initial CTD casts.

Details of the M21 method are given in the Supporting Information S1, however the key assumptions are as follows.

1. Turbulence occurs due to double-diffusive convection
2. Spatial variations in temperature and salinity that are not resolved by measurements are dominated by stirring along isopycnals, so gradients in spice s_p are much larger than gradients in density $\rho = \rho_0 - \alpha T + \beta S$ at small scales

To complete the method, a model power spectrum for spice variance associated with along-isopycnal stirring is required. Middleton, Fine, et al. (2021) use the form $E_{s_p} = A\tilde{k}^{-1}$, where $\tilde{k}$ is the wavenumber magnitude in coordinates stretched by a factor of N/f in the vertical ($N = \sqrt{\partial\overline{b}/\partial z}$ is the buoyancy frequency and f is the Coriolis parameter). Middleton, Fine, et al. (2021) verify that the vertical to horizontal aspect ratio for spice gradients in the Arctic ocean is close to N/f; however, resolution constraints prevented them from directly assessing the wavenumber scaling $\tilde{k}^{-1}$. In our mooring data, we have a range of scales of temperature variation, and as spice s_p is dominated by temperature, we can gain some clues about the scaling of spice. Based on CTD data N/f varies between 100 and 200 in the upper 2 m, which is comparable to a median value of 124 for the ratio between $\frac{\partial\overline{T}}{\partial z}$ and $\frac{\partial\overline{T}}{\partial x}$ measured by the upper thermistor (initially at 0.5 m depth). Vertical temperature gradients are calculated using a vertically spaced pair of thermistors, and horizontal gradients are calculated by advecting temperature measurements laterally using the mean flow speed $\overline{u}$ (applying the frozen field hypothesis). The deeper thermistor (initially at 20.5 m) averages $\frac{\partial\overline{T}}{\partial z} \sim 10\frac{\partial\overline{T}}{\partial x}$ which is a little lower than the values of N/f between 20 and 30 at ∼20 m depth. These values indicate that the N/f aspect ratio is a reasonable assumption.

In Figure 3e we show data from the lower turbulence instrument cluster, which included a high resolution MicroSquid FP07 temperature sensor. Plotting the power spectra averaged by mean flow speed against wavenumber (applying the frozen field hypothesis), we find a k^{-1} slope at low wavenumbers, consistent with a $\tilde{k}^{-1}$ slope in the spice variance spectrum. In Figure 3f we show the frequency spectrum for the thermistor data. The thermistors sample every 5 min, giving a large coverage in frequency space over the year-long mooring. The frozen field hypothesis can only be applied over relatively short time periods, so we do not plot the wavenumber power spectra for the thermistors. However, at high frequencies where the frozen field hypothesis is valid, the wavenumber variation should be similar to the frequency variation. The spectral slope transitions from a f^{-2} scaling to a f^{-1} scaling in both thermistors, potentially due to temporal changes in temperature rather than spatial ones. However, a f^{-1} slope at high frequencies is consistent with our model $\tilde{k}^{-1}$ spice variance spectrum for sub-thermistor scales.

The simplified expression for the dissipation rate in the M21 method is

$$\overline{\epsilon} = \left(\frac{1}{\sqrt{6}}\pi g\left(\kappa_T - \kappa_S\right)\frac{\overline{|\nabla b|}}{b_z^*}\sqrt{A}\right)^{\frac{2}{3}} N, \tag{4}$$

where, A represents the magnitude of spice variance estimated using the two point correlation $R(\tilde{r}) = \overline{|s_p(\mathbf{x},t) - s_p(\mathbf{x}+\tilde{r}\mathbf{a},t)|^2}$ with stretched coordinate $\tilde{r}$ taken along isopycnals. The method inputs are the buoyancy gradient $|\nabla b|$ (estimated as the buoyancy frequency squared $N^2 = \partial\overline{b}/\partial z$ shown in Figure 1e), the sorted buoyancy gradient b_z^*, and the two-point correlation for spice variance $R(\tilde{r})$. The mooring contained no salinity sensors, so we rely on temperature sensors and initial CTD T/S relationship to determine salinity for calculations of buoyancy and spice.

We compare the M21 method with the observed dissipation rates in Figure 4. The M21 method is inherently statistical, so we expect some spread around the predicted dissipation. The mean dissipation rate estimated from the M21 method is within a factor of 1.15 and 1.20 of measured values at the lower and upper MAVS, respectively. The variation in dissipation rate at both upper and lower MAVS is also captured, with the predicted standard deviation within a factor of 1.08 of the observed standard deviation for both MAVS. We also capture the difference in dissipation rate between the upper and lower MAVS, suggesting that our method has predictive skill.

Our method underestimates the dissipation rate when the buoyancy Reynolds number $Re_b = \epsilon/\nu N^2 > 20$, consistent with the application of the method to data from the Arctic as reported in Middleton, Fine, et al. (2021). The periods of high Re_b are associated with an order of magnitude larger dissipation rate (on average 1.3×10^{-9} m^{2}s^{-3} compared with 1.5×10^{-10} m^{2}s^{-3} at the upper MAVS). This could indicate that when $Re_b > 20$, double diffusion

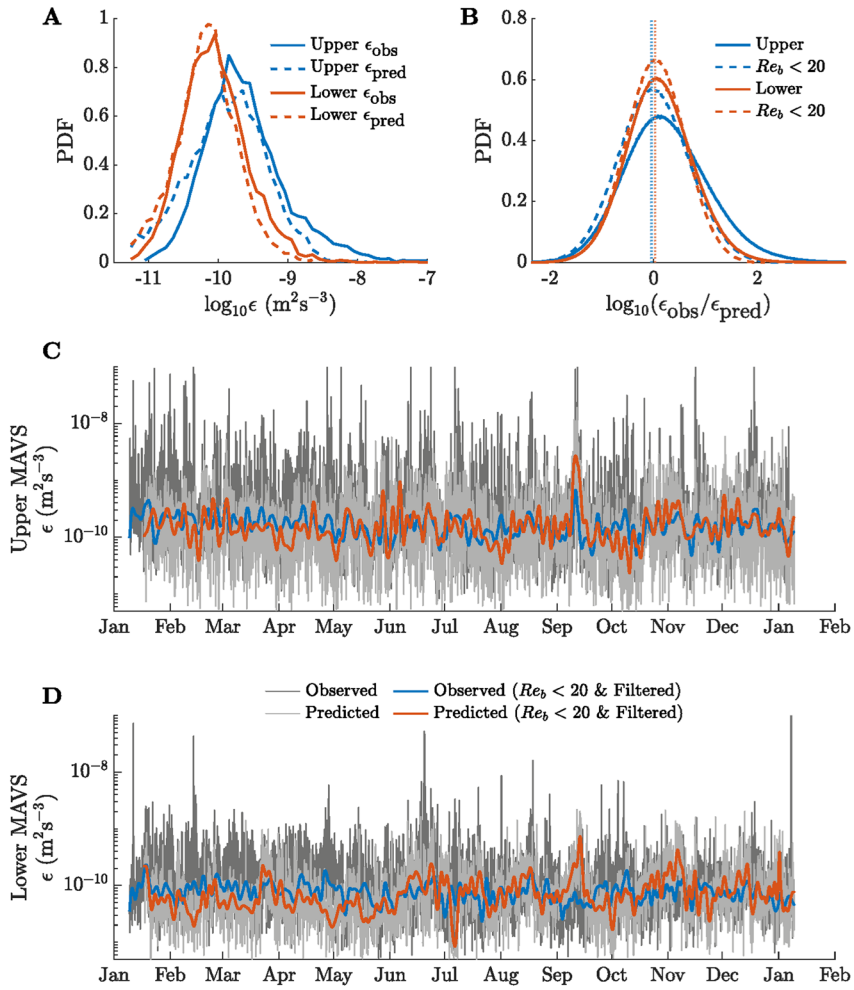

Figure 4. (a) PDFs of upper and lower Modular Acoustic Velocity Sensors (MAVS) observed dissipation rate and predicted dissipation rate. (b) PDF of the log of the ratio between observed and predicted dissipation rate. (c) Timeseries of observed and predicted dissipation rates for upper MAVS, along with filtered signal without high $Re_b > 20$ data. (d) Same as C for lower MAVS data.

is not the only driver of turbulence. However, the majority of points in our data set have $Re_b < 20$; at the upper MAVS, $Re_b > 20 \sim 21\%$ of the time and at the lower MAVS, $Re_b > 20$ only ~9% of the time. Similar intermittent behavior is also observed in the microstructure profiles presented in Venables et al. (2014). Some CTD profiles show a strong staircase structure concurrent with low dissipation rates ($2{-}4 \times 10^{-10}$ m^2s^{-3}), whereas others show no staircase structure and elevated dissipation rates ($2{-}3 \times 10^{-8}$ m^2s^{-3}). In the Larsen C data, values of Re_b are at least $\mathcal{O}(1000)$ (Davis & Nicholls, 2019), providing a clear distinction between the two regimes. However, in the GVIIS data, the Re_b values do not correlate with mean flow speed (not shown), suggesting that the points with $Re_b > 20$ might be associated with internal wave breaking rather than shear-driven boundary layer turbulence. Internal wave breaking may explain the more sporadic bursts of high Re_b turbulence, rather than a consistently elevated Re_b, as observed beneath Larsen C (Davis & Nicholls, 2019). However, as shown in Vreugdenhil and Taylor (2019), strongly stratified shear-driven turbulence in the ice shelf-ocean boundary layer can also provide intermittent bursts of turbulence. Further investigation is required to isolate the driver of the $Re_b > 20$ events.

4. Heat Flux

Heat and salt fluxes driven by turbulence, are responsible for the observed basal melting. To estimate the turbulent heat flux, $\overline{w'T'}$, we use a direct measurement of the dissipation of thermal variance, $\chi_T = \kappa_T \overline{|\nabla T|^2}$, from the lower MicroSquid sensor, and apply the method of Osborn and Cox (1972) that assumes $\chi_T = 2\overline{w'T'}\frac{\partial \overline{T}}{\partial z}$. We

estimate χ_T by fitting a k^{-1} slope to the temperature power spectra in Figure 3e using a viscous-convective range scaling (Batchelor, 1953; see Supporting Information S1 for details). The heat flux estimate at the lower instrument is 3.2 ± 0.8 Wm^{-2}, which corresponds to a melt rate of 0.33 ± 0.08 m yr^{-1} (± denotes a standard deviation in χ_T), lower than the observed 1.4 m yr^{-1} (13.7 Wm^{-2}).

At the upper instrument, the MicroSquid sensor failed. However, if we assume that double-diffusive convection drives turbulence, then we can equate the turbulent buoyancy flux to the dissipation rate that is, $\overline{w'b'} = \epsilon$. Relating the turbulent heat flux to the turbulent buoyancy flux requires an estimate of the flux ratio $\gamma = \alpha\overline{w'T'}/\beta\overline{w'S'}$ via $\overline{w'b'} = \alpha\overline{w'T'}\left(1-\gamma^{-1}\right)$. We calculate γ at the lower instrument by equating our two estimates for $\overline{w'T'}$ from χ_T and ϵ. This gives a value for γ of between 0.26 and 0.43, providing a close fit between the ϵ-based estimate of the heat flux and the χ_T-based estimate at the lower MAVS. Using the mean γ from the lower instrument gives a heat flux at the upper instrument of 9.6 ± 2.4 Wm^{-2} (± denotes a standard deviation in γ) which corresponds to a melt rate of 0.98 ± 0.28 m yr^{-1}, still lower than the observed 1.4 m yr^{-1}.

Variation in γ is dependant on the mean flow speed, visible in the changing temperature spectra with mean flow (pictured in the spectra in Figure 3e), despite no change in the dissipation rate (Figures 2b and 2c). Changes in γ with mean flow speed suggest that the mean flow may still affect the heat flux and melt rate, despite not controlling the rates of turbulence. However, the effect of changes in γ on heat flux are modest compared with the variations driven by a changing dissipation rate. The variations in γ contribute to a standard deviation in the heat flux of about 0.8 Wm^{-2} at the lower MAVS and 2.4 Wm^{-2} at the upper MAVS. However, the variance in ϵ contributes changes in the heat flux on the order of a factor of three; a log-normal standard deviation in ϵ contributes variance between 1.2 and 8.9 Wm^{-2} at the lower MAVS and between 3.6 and 35.6 Wm^{-2} at the upper MAVS. The variance in dissipation rate is not correlated with the mean flow-speed, so the majority of heat flux variance is also not explained by changes in the mean flow-speed, but can be explained by the effect of double-diffusive convection shown in Figure 4.

The increase in predicted dissipation rates from the lower instrument to the upper instrument is due to both an increase in the lateral gradients in temperature, giving a larger value of A in Equation 4, and to an increase in stratification. The term $|\nabla b|/b_z^*$ in Equation 4, which we approximate as N^2/b_z^*, gives a measure of spatial variations in isopycnals; flat isopycnals would give a value of $N^2/b_z^* = 1$. Both factors in Equation 4 that depend on buoyancy, $(|\nabla b|/b_z^*)^{2/3}$ and N, are larger at the upper instrument, contributing to the larger dissipation rate. Although the heat flux at the upper instrument is insufficient to cause the observed melting, we know from the initial CTD profiles that the stratification increases closer to the ice, giving a larger value of N (see Figure 1e). The variance in temperature also increases, which is visible in the difference between the temperature spectra at 0.5 and 20.5 m in Figure 3f. An increase in temperature variance implies an increase in the spice variance magnitude A and potentially an increase in buoyancy variations and N^2/b_z^*. Therefore, we may expect larger rates of turbulence closer to the ice and a larger heat flux, perhaps sufficient to match the observed melt rate. In order to maintain a statistically steady state, a larger vertical heat flux closer to the ice must be balanced by a divergence in the horizontal lateral flux.

5. Conclusions

In this letter, we analyzed turbulence data from a year-long mooring beneath GVIIS, at a location where intermittent thermohaline-layering was previously observed (Kimura et al., 2015; Venables et al., 2014). We showed in Section 2 that the observed dissipation rate does not depend on the mean flow speed at this location, in contrast to the notion of a shear-driven boundary layer that has been observed at other under-ice shelf locations (Davis & Nicholls, 2019; Jenkins et al., 2010). Instead, we found that double-diffusive convection can explain the observed dissipation rates. Using the method from Middleton, Fine, et al. (2021) in Section 3, we related the observed dissipation rates to large scale variations in along-isopycnal temperature, which are hypothesized to generate small scale gradients in spice that drive double-diffusive convection. The intensity of double-diffusive convection predicted by the M21 method increases with stratification and temperature variance, and in Section 4 we found an increase in heat flux toward the ice, consistent with the stronger stratification and temperature variance. The predominant variation in heat flux, and so melt rate, appears to be associated with changes in turbulence driven by horizontal spice variance, rather than the mean flow speed.

Our observations suggest that in locations where stratification is strong, leading to a low buoyancy Reynolds number $Re_b = \epsilon/\nu N^2 < 20$, along-isopycnal spice variance might be a better indicator of basal melting than the flow speed. Beneath George VI Ice Shelf, this strong stratification is caused by the warm and salty Circumpolar Deep Water, which is believed to be responsible for the recent enhancement of ice mass loss on the West Antarctic Peninsula (Jenkins et al., 2018). Modeling studies that rely on the three-equation formalism to predict melt rates in regions of strong stratification could fail to capture the relationship between the ocean state and the basal melt rate. It is not yet clear how prevalent double-diffusive ice-ocean boundary layers are, because of the limited number of borehole observations, so we recommend further process studies on the transition between double-diffusive and shear-driven boundary layers. However, our work suggests that a parameterization of the double-diffusive boundary layer could be developed based on far-field stratification and isopycnal spice variance.

Data Availability Statement

Mooring data are available for download at the Polar Data Centre (https://doi.org/10.5285/C4A8AD33-2C09-44E9-B4EA-2923BB4B85F1).

Acknowledgments
The authors gratefully acknowledge helpful feedback from the ISOBL project team, as well as from two anonymous reviewers, whose comments helped improve this manuscript. This work was funded by a grant from the Natural Environment Research Council, NE/L002507/1.

References

Batchelor, G. K. (1953). *The theory of homogeneous turbulence*. Cambridge university press.
Begeman, C. B., Tulaczyk, S. M., Marsh, O. J., Mikucki, J. A., Stanton, T. P., Hodson, T. O., et al. (2018). Ocean stratification and low melt rates at the Ross Ice Shelf grounding zone. *Journal of Geophysical Research: Oceans*, *123*(10), 7438–7452. https://doi.org/10.1029/2018jc013987
Bishop, J., & Walton, J. (1981). Bottom melting under George VI Ice Shelf, Antarctica. *Journal of Glaciology*, *27*(97), 429–447. https://doi.org/10.1017/s0022143000011461
Bluteau, C. E., Jones, N. L., & Ivey, G. N. (2011). Estimating turbulent kinetic energy dissipation using the inertial subrange method in environmental flows. *Limnology and Oceanography: Methods*, *9*(7), 302–321. https://doi.org/10.4319/lom.2011.9.302
Corr, H. F., Jenkins, A., Nicholls, K. W., & Doake, C. (2002). Precise measurement of changes in ice-shelf thickness by phase-sensitive radar to determine basal melt rates. *Geophysical Research Letters*, *29*(8), 73–74. https://doi.org/10.1029/2001gl014618
Dadonau, M., Partridge, J., & Linden, P. (2020). The effect of double diffusion on the dynamics of horizontal turbulent thermohaline jets. *Journal of Fluid Mechanics*, *905*. https://doi.org/10.1017/jfm.2020.744
Davis, P. E., & Nicholls, K. W. (2019). Turbulence observations beneath Larsen C Ice Shelf, Antarctica. *Journal of Geophysical Research: Oceans*, *124*(8), 5529–5550. https://doi.org/10.1029/2019jc015164
Dinniman, M. S., Asay-Davis, X. S., Galton-Fenzi, B. K., Holland, P. R., Jenkins, A., Timmermann, R., & Timmermann, R. (2016). Modeling ice shelf/ocean interaction in Antarctica: A review. *Oceanography*, *29*(4), 144–153. https://doi.org/10.5670/oceanog.2016.106
Fer, I., & Sundfjord, A. (2007). Observations of upper ocean boundary layer dynamics in the marginal ice zone. *Journal of Geophysical Research*, *112*(C4), C04012. https://doi.org/10.1029/2005jc003428
Hellmer, H. H., & Olbers, D. J. (1989). A two-dimensional model for the thermohaline circulation under an ice shelf. *Antarctic Science*, *1*(4), 325–336. https://doi.org/10.1017/s0954102089000490
Holland, D. M., & Jenkins, A. (1999). Modeling thermodynamic ice-ocean interactions at the base of an ice shelf. *Journal of Physical Oceanography*, *29*(8), 1787–1800. https://doi.org/10.1175/1520-0485(1999)029<1787:mtioia>2.0.co;2
Jenkins, A., & Jacobs, S. (2008). Circulation and melting beneath George VI Ice Shelf, Antarctica. *Journal of Geophysical Research*, *113*(C4), C04013. https://doi.org/10.1029/2007jc004449
Jenkins, A., Nicholls, K. W., & Corr, H. F. (2010). Observation and parameterization of ablation at the base of Ronne Ice Shelf, Antarctica. *Journal of Physical Oceanography*, *40*(10), 2298–2312. https://doi.org/10.1175/2010jpo4317.1
Jenkins, A., Shoosmith, D., Dutrieux, P., Jacobs, S., Kim, T. W., Lee, S. H., et al. (2018). West Antarctic ice sheet retreat in the Amundsen sea driven by decadal oceanic variability. *Nature Geoscience*, *11*(10), 733–738. https://doi.org/10.1038/s41561-018-0207-4
Kimura, S., Nicholls, K. W., & Venables, E. (2015). Estimation of ice shelf melt rate in the presence of a thermohaline staircase. *Journal of Physical Oceanography*, *45*(1), 133–148. https://doi.org/10.1175/jpo-d-14-0106.1
Konopliv, N., & Meiburg, E. (2016). Double-diffusive lock-exchange gravity currents. *Journal of Fluid Mechanics*, *797*, 729–764. https://doi.org/10.1017/jfm.2016.300
Lindborg, E. (2006). The energy cascade in a strongly stratified fluid. *Journal of Fluid Mechanics*, *550*, 207. https://doi.org/10.1017/s0022112005008128
Locarnini, M., Mishonov, A., Baranova, O., Boyer, T., Zweng, M., & Garcia, H. (2018). World ocean atlas 2018, Volume 1: Temperature.
Malyarenko, A., Wells, A. J., Langhorne, P. J., Robinson, N. J., Williams, M. J., & Nicholls, K. W. (2020). *A synthesis of thermodynamic ablation at ice-ocean interfaces from theory, observations and models*. Ocean Modelling.
McPhee, M. (2008). *Air-ice-ocean interaction: Turbulent ocean boundary layer exchange processes*. Springer Science & Business Media.
McPhee, M. G., Maykut, G. A., & Morison, J. H. (1987). Dynamics and thermodynamics of the ice/upper ocean system in the marginal ice zone of the Greenland Sea. *Journal of Geophysical Research*, *92*(C7), 7017–7031. https://doi.org/10.1029/jc092ic07p07017
Middleton, L., Fine, E., MacKinnon, J., Alford, M., & Taylor, J. (2021). Estimating dissipation rates associated with double diffusion. *Geophysical Research Letters*, *48*, e2021GL092779. https://doi.org/10.1029/2021gl092779
Middleton, L., & Taylor, J. R. (2020). A general criterion for the release of background potential energy through double diffusion. *Journal of Fluid Mechanics*, *893*. https://doi.org/10.1017/jfm.2020.259
Middleton, L., Vreugdenhil, C. A., Holland, P. R., & Taylor, J. R. (2021a). Numerical simulations of melt-driven double-diffusive fluxes in a turbulent boundary layer beneath an ice shelf. *Journal of Physical Oceanography*, *51*(2), 403–418. https://doi.org/10.1175/jpo-d-20-0114.1
Moffat, C., Owens, B., & Beardsley, R. (2009). On the characteristics of circumpolar deep water intrusions to the west antarctic peninsula continental shelf. *Journal of Geophysical Research*, *114*(C5), 7017–7031. https://doi.org/10.1029/2008jc004955

Monin, A. S., & Obukhov, A. M. (1954). Basic laws of turbulent mixing in the surface layer of the atmosphere. *Contributions of the Geophysical Institute of the Academy of Sciences of the USSR*, *151*(163), e187.

Morlighem, M., Rignot, E., Binder, T., Blankenship, D., Drews, R., Eagles, G., et al. (2020). Deep glacial troughs and stabilizing ridges unveiled beneath the margins of the Antarctic ice sheet. *Nature Geoscience*, *13*(2), 132–137. https://doi.org/10.1038/s41561-019-0510-8

Osborn, T. R., & Cox, C. S. (1972). Oceanic fine structure. *Geophysical Fluid Dynamics*, *3*(4), 321–345. https://doi.org/10.1080/03091927208236085

Potter, J. R., & Paren, J. G. (1985). Interaction between ice shelf and ocean in George VI sound, Antarctica. *Oceanology of the Antarctic continental shelf*, *43*, 35–58. https://doi.org/10.1029/ar043p0035

Rignot, E., Mouginot, J., Scheuchl, B., Van Den Broeke, M., Van Wessem, M. J., & Morlighem, M. (2019). Four decades of Antarctic ice sheet mass balance from 1979–2017. *Proceedings of the National Academy of Sciences*, *116*(4), 1095–1103. https://doi.org/10.1073/pnas.1812883116

Rosevear, M. G., Gayen, B., & Galton-Fenzi, B. K. (2021). The role of double-diffusive convection in basal melting of Antarctic ice shelves. *Proceedings of the National Academy of Sciences*, *118*(6). https://doi.org/10.1073/pnas.2007541118

Stevens, C., Hulbe, C., Brewer, M., Stewart, C., Robinson, N., Ohneiser, C., & Jendersie, S. (2020). Ocean mixing and heat transport processes observed under the Ross Ice Shelf control its basal melting. *Proceedings of the National Academy of Sciences*, *117*(29), 16799–16804. https://doi.org/10.1073/pnas.1910760117

Venables, E., Nicholls, K., Wolk, F., Makinson, K., & Anker, P. (2014). Measuring turbulent dissipation rates beneath an Antarctic ice shelf. *Marine Technology Society Journal*, *48*(5), 18–24. https://doi.org/10.4031/mtsj.48.5.8

Vreugdenhil, C. A., & Taylor, J. R. (2019). Stratification effects in the turbulent boundary layer beneath a melting ice shelf: Insights from resolved large-eddy simulations. *Journal of Physical Oceanography*, *49*(7), 1905–1925. https://doi.org/10.1175/jpo-d-18-0252.1

References From the Supporting Information

McDougall, T. J., & Barker, P. M. (2011). Getting started with teos-10 and the Gibbs seawater (GSW) oceanographic toolbox. *SCOR/IAPSO WG*, *127*, 1–28.

Riley, J. J., & Lindborg, E. (2008). Stratified turbulence: A possible interpretation of some geophysical turbulence measurements. *Journal of the Atmospheric Sciences*, *65*(7), 2416–2424.

Sharqawy, M., Lienhard, J., & Zubair, S. (2010). Thermophysical properties of seawater: A review of existing correlations and data. *Desalination and Water Treatment*, *16*(1–3), 354–380.

Thwaites, F., & Williams, A. (1996). Development of a modular acoustic velocity sensor. In *Oceans 96 MTS/IEEE conference proceedings, the Coastal Ocean-prospects for the 21st Century* (Vol. 2, pp. 607–612).

Tseng, Y.-h., & Ferziger, J. H. (2001). Mixing and available potential energy in stratified flows. *Physics of Fluids*, *13*(5), 1281–1293.

Vitagliano, V., & Lyons, P. A. (1956). Diffusion coefficients for aqueous solutions of sodium chloride and barium chloride. *Journal of the American Chemical Society*, *78*(8), 1549–1552.